Bulletin of the Seismological Society of America, Vol. 106, No. 3, pp. –, June 2016, doi: 10.1785/0120150211

Ⓔ

Discriminating Characteristics of Tectonic and Human-Induced Seismicity

by Ilya Zaliapin and Yehuda Ben-Zion

Abstract We analyze statistical features of background and clustered subpopulations of earthquakes in different regions in an effort to distinguish between human-induced and natural seismicity. Analysis of end-member areas known to be dominated by human-induced earthquakes (The Geyser geothermal field in northern California and TauTona gold mine in South Africa) and regular tectonic activity (the San Jacinto fault zone in southern California and the Coso region, excluding the Coso geothermal field in eastern central California) reveals several distinguishing characteristics. Induced seismicity is shown to have (1) higher rate of background events (both absolute and relative to the total rate), (2) faster temporal offspring decay, (3) higher rate of repeating events, (4) larger proportion of small clusters, and (5) larger spatial separation between parent and offspring, compared to regular tectonic activity. These differences also successfully discriminate seismicity within the Coso and Salton Sea geothermal fields in California before and after the expansion of geothermal production during the 1980s.

Online Material: Figures of examined regions, earthquake epicenters, and joint distributions of the time and space components of the nearest-neighbor distance.

Introduction

The current boom in the practice of induced fracturing (fracking) in oil and gas production and associated fluid waste disposal have led to increased awareness of human-induced earthquakes (Suckale, 2010; Horton, 2012; Ellsworth, 2013; Keranen *et al.*, 2013; Hauksson *et al.*, 2015), although the problem has been known for decades (e.g., McGarr *et al.*, 2002, and references therein). The recent well-documented increase in seismicity in the midwestern United States (Ellsworth, 2013), as well as earthquakes in Basel and St. Gallen in Switzerland and other areas with geothermal production (Suckale, 2010), further emphasize the elevated risks posed by induced seismicity. The risk may be especially hard to assess in tectonically active regions such as California (McGarr, 1991), where many active oil and gas production fields are located next to highly populated urban areas, including Los Angeles.

Quantitative assessment of the hazards associated with induced seismicity is complicated by the fact that, hampered by the general earthquake complexity, standard seismological methods fail to discriminate between induced and natural tectonic earthquakes (e.g., in terms of stress drop, moment release, mechanism, etc.). This study addresses the discrimination problem by focusing on statistical features of seismic clusters, as opposed to properties of individual events. We document several differences between the space–time distributions of the clustered and background parts of seismicity in regions of natural versus human-induced activity. Specifically, we analyze the distribution of space–time distances between pairs of nearest-neighbor earthquakes, referred to as cluster style. We examine data in four regions with a clear-cut dominant tectonic or human-related driver of seismicity and two additional regions with mixed activity. The latter two regions experienced development of geothermal production during the instrumental period, which is reflected in temporal evolution of cluster style in these areas. The well-documented geothermal production or mining activity (or absence of such), together with availability of high-quality catalogs and detailed geological and/or geochemical studies in the examined regions, provide good platforms for testing hypotheses about possible similarities and differences between natural and induced seismicity.

To identify earthquake nearest neighbors and clarify the cluster style of a given region, we use the seismic cluster techniques that were shown useful for identification and classification of statistically significant seismicity clusters in southern California in relation to the physical properties of the crust (Zaliapin *et al.*, 2008; Zaliapin and Ben-Zion, 2011, 2013a,b; Gu *et al.*, 2013). In the next section, we outline basic properties of the regions and the data used in this work. The Earthquake Nearest Neighbors section summarizes key aspects of the employed seismic cluster techniques.

Table 1
Seismicity Used in the Study

Region	Period (yyyy/mm)	Magnituge Range	Number of Events	Type of Seismicity
The Geysers, California	1984/01–2011/12	1.0–4.5	75,991	Induced
TauTona gold mine, South Africa	2004/09–2010/09	1.5–4.2	8519	Induced
Coso geothermal field, California	1981/01–2013/12	1.0–4.41	4412	Mixed
Salton Sea geothermal field, California	1981/01–2013/12	1.5–5.11	6018	Mixed
Coso nongeothermal area, California	1981/01–2013/12	1.0–5.75	56,801	Tectonic
San Jacinto fault zone, California	1981/01–2013/12	1.0–5.43	39,768	Tectonic

The results are described, interpreted, and discussed in the Results and Discussion sections.

Regions and Data

We work with seismic catalogs of six regions (see Table 1 and Ⓔ Figures S1 and S2, available in the electronic supplement to this article, for summaries of the examined seismicity and related maps). (1) The Geysers geothermal field in northern California is dominated by induced seismicity caused by operation of the world's largest complex of 22 geothermal power plants, with over 350 production wells. The seismicity before operation of the geothermal plants in this area was negligible. Since the beginning of routine earthquake recording in May 1975, the seismicity closely follows the power production and concentrates in the vicinity of the producing steam wells (Marks *et al.*, 1978; Eberhart-Phillips and Oppenheimer, 1984; Oppenheimer, 1986; Majer and Peterson, 2007). (2) The TauTona gold mine in South Africa, which is one of the deepest and best-investigated operating mines worldwide (Boettcher *et al.*, 2009, 2015; Lippmann-Pipke *et al.*, 2011), is located in a tectonically dormant region (the Kaapvaal craton) about 90 km southwest of Johannesburg and the seismicity in the mine is primarily associated with blasting activity. We refer to Boettcher *et al.* (2015) for further detail on this region and the examined catalog. (3) The Coso geothermal field in the eastern portion of central California has operated continuously since 1987 and currently has over 150 wells. Located within the Walker Lane transition zone, the region has a noticeable level of natural seismicity, which is recorded in the examined catalog for 1981–1987. After 1987 the seismicity in this area likely presents a mixture of natural and human-induced earthquakes. Hauksson and Unruh (2007) review the regional tectonics and seismic patterns in the Coso geothermal area. (4) The Salton Sea geothermal field, located in the Brawley seismic zone of the San Andreas system in southern California near the southern shore of the Salton Sea, started in 1982 and was greatly expanded during 1988–1992 (Brodsky and Lajoie, 2013). The region had significant seismicity prior to geothermal production and currently presents a mixture of natural and induced earthquakes. (5) The larger Coso region in central California, excluding the Coso geothermal field, has a moderate level of seismicity with no geothermal production or mining. (6) The San Jacinto fault zone in southern California is currently the most seismically active fault zone in southern California, and it has no geothermal or mining activities.

The seismic data of the Coso geothermal and nongeothermal areas, Salton Sea geothermal area, and San Jacinto fault zone are taken from the 1981–2014 relocated catalog of Hauksson *et al.* (2012). The seismicity of The Geysers geothermal field is taken from the 1981–2012 relocated catalog of Waldhauser and Schaff (2008). The seismic data of the TauTona mine is an updated catalog over 2004–2010 (M. Boettcher, personal comm., 2015) from Boettcher *et al.* (2009). The lowest considered magnitude in The Geysers, Coso, and San Jacinto areas is m_c 1; and, in the TauTona and Salton Sea areas, it is m_c 1.5. The minimal examined magnitude is below the completeness magnitude for some analyzed spatiotemporal areas. This does not affect the main results and conclusions of the study, because the cluster structure estimated by our method is insensitive to the minimal reported magnitude and catalog incompleteness, as was illustrated with epidemic-type aftershock sequence simulations and analysis of real seismicity by Zaliapin and Ben-Zion (2013a, section 2.2, Supporting Information Sections D and E). Including small events below the completeness magnitude enables more detailed (albeit incomplete) analysis of small regions of interest (e.g., Vidale and Shearer, 2006; Chen *et al.*, 2012; Brodsky and Lajoie, 2013; Zaliapin and Ben-Zion, 2015).

Earthquake Nearest Neighbors

The main tool of our cluster analysis is a particular distance between earthquakes introduced by Baiesi and Paczuski (2004) that combines information in the space–time–magnitude coordinates. This is used for each earthquake to identify its earlier nearest neighbor, referred to as the parent. Specifically, if event i is characterized by occurrence time t_i, hypocenter (ϕ_i, λ_i, d_i), and magnitude m_i, then the proximity of earthquake j to earthquake i is asymmetric in time and is defined as (Baiesi and Paczuski, 2004)

$$\eta_{ij} = \begin{cases} t_{ij}(r_{ij})^d 10^{-bm_i}, & t_{ij} > 0; \\ \infty, & t_{ij} \le 0. \end{cases} \quad (1)$$

Here, $t_{ij} = t_j - t_i$ is the event intercurrence time, which is positive if event j occurred after event i; $r_{ij} \ge 0$ is the spatial distance between the earthquake hypocenters; d is the (possibly fractal) dimension of the hypocenters; and b is the

parameter (referred to as b-value) of the Gutenberg–Richter law that approximates the observed number $N(m)$ of events with magnitude above m:

$$\log_{10} N(m) = a - bm, \qquad m \geq m_c. \tag{2}$$

This definition of the distance is motivated by the following observation. Consider a marked spatiotemporal point field $P(t, \mathbf{x})$ that is stationary in time t, possibly inhomogeneous in space $\mathbf{x}$, has the fractal dimension d of its space projection, and has marks (event magnitudes) distributed according to the Gutenberg–Richter law of equation (2). The space and time coordinates are independent, and the event marks are independent of the coordinates. Consider also the spatiotemporal volume V_{ij} between event j and an earlier event i, defined as the space–time cylinder whose space projection is the sphere $S(i, r_{ij})$ centered at j with radius r_{ij} and the temporal projection is the interval $[t_i, t_j]$:

$$V_{ij} = S(i, r_{ij}) \times [t_i, t_j]. \tag{3}$$

Then η_{ij} is proportional (or equal, under a proper choice of process intensity) to the expected number of events with magnitude above m_j that are observed within volume V_{ij} in the process P:

$$\eta_{ij} \propto E[P(V_{ij}|m > m_j)] = \int_{V_{ij}} I_{\{m>m_i\}} P(dt, d\mathbf{x})$$
$$= \lambda \int_{S(i,r_{ij})} P(d\mathbf{x}) \int_{[t_i,t_j]} I_{\{m>m_i\}} dt = \lambda (r_{ij})^d t_{ij} 10^{-bm_j}, \tag{4}$$

in which $P(dt, d\mathbf{x}) = \lambda P(d\mathbf{x})dt$ is the counting measure of the process with intensity λ, and $E[X]$ denotes the mathematical expectation with respect to this counting measure (Daley and Vere-Jones, 2007).

Intuitively, this approach defines a generalized earthquake distance between any pair of events to be equal to the expected number of points observed between these events in a time-homogeneous process. This is exactly how the conventional Euclidean distance can be defined in n-dimensional space R^n if process P is a stationary point process in this space. Other properties of this distance and its further connection to the Euclidean metric are discussed in Zaliapin *et al.* (2008) and Zaliapin and Ben-Zion (2013a).

Consider the space and time distances between event i and its parent j normalized by the magnitude of the parent event (Zaliapin *et al.*, 2008):

$$T_{ij} = t_{ij} 10^{-qbm_i}; \qquad R_{ij} = (r_{ij})^d 10^{-pbm_i}; \qquad p + q = 1. \tag{5}$$

This is convenient because now $\log \eta_{ij} = \log T_{ij} + \log R_{ij}$. For each event j, we identify its unique nearest neighbor (parent) i with respect to the distance of equation (1) and, for simplicity, denote the nearest-neighbor distance by the same symbol η_{ij}. The event j is called an offspring of i. According to this definition, each event (except the first event in the catalog) has a unique parent and also may have multiple offspring.

Zaliapin *et al.* (2008) and Zaliapin and Ben-Zion (2013a) demonstrated that a time-stationary space-inhomogeneous Poisson flow of events with Gutenberg–Richter magnitudes corresponds to a unimodal distribution of $(\log T, \log R)$ that is concentrated along a line $\log_{10} T + \log_{10} R =$ constant. Observed seismicity, however, shows a bimodal joint distribution of $(\log_{10} T, \log_{10} R)$. One mode corresponds to background events (similar to that of a Poisson process), whereas the other consists of clustered events located considerably closer in time and space to their parents than expected in a Poisson process (see Fig. 1). A suitably chosen nearest-neighbor threshold η_0 can be used to formally attribute each event to either the background (if $\eta_{ij} > \eta_0$) or cluster (if $\eta_{ij} < \eta_0$) mode.

In this study, we use event epicenters rather than hypocenters, because the depth coordinates are often less accurate than those of the epicenters and location errors lead to various analysis artifacts, as discussed in detail by Zaliapin and Ben-Zion (2015). To ensure that this choice does not change the essential aspects of the results, we repeated the analyses of this study with event hypocenters (not shown) and found that the 3D results are very close to the 2D results shown below. This is because clustered events occupy a very narrow spatiotemporal domain around their parents; the total volume of this domain is orders of magnitude below that of the background events (see Zaliapin and Ben-Zion, 2013a, for further discussion). Accordingly, the cluster-background separation can be effectively done with epicenters rather than hypocenters. In addition, we fix $b = 1$, $d = 1.6$, and $p = 0.5$. Zaliapin and Ben-Zion (2013a) showed that the estimated cluster structure is fairly robust with respect to the values of these parameters, so our main conclusions are not sensitive to the precise parameter values. We refer to Zaliapin and Ben-Zion (2013a) for further details on and examples of performance of the technique.

Results

Cluster Style of Tectonic Versus Induced Areas

Figure 1 shows the 2D joint distributions of the rescaled time and space components (T, R) of the nearest-neighbor earthquake distance η for the six examined regions (see the Regions and Data section and Ⓔ Figs. S1 and S2 for region description). Each point in these plots corresponds to a catalog event; its location in the (T, R) plane provides information about the time and space distance to the event's parent. The magnitude range of the examined seismicity in each region is indicated in Table 1. The normalization (equation 5) of the original times t and distances r to parent by the parent magnitude ensures that the clouds of points that correspond to offspring of events of different magnitudes closely overlap (without this normalization, the offspring of an M 3 event would spread wider in time and space than the offspring of an M 2 event, etc.).

All six regions exhibit background and clustered modes of seismicity, with different degrees of mode separation and

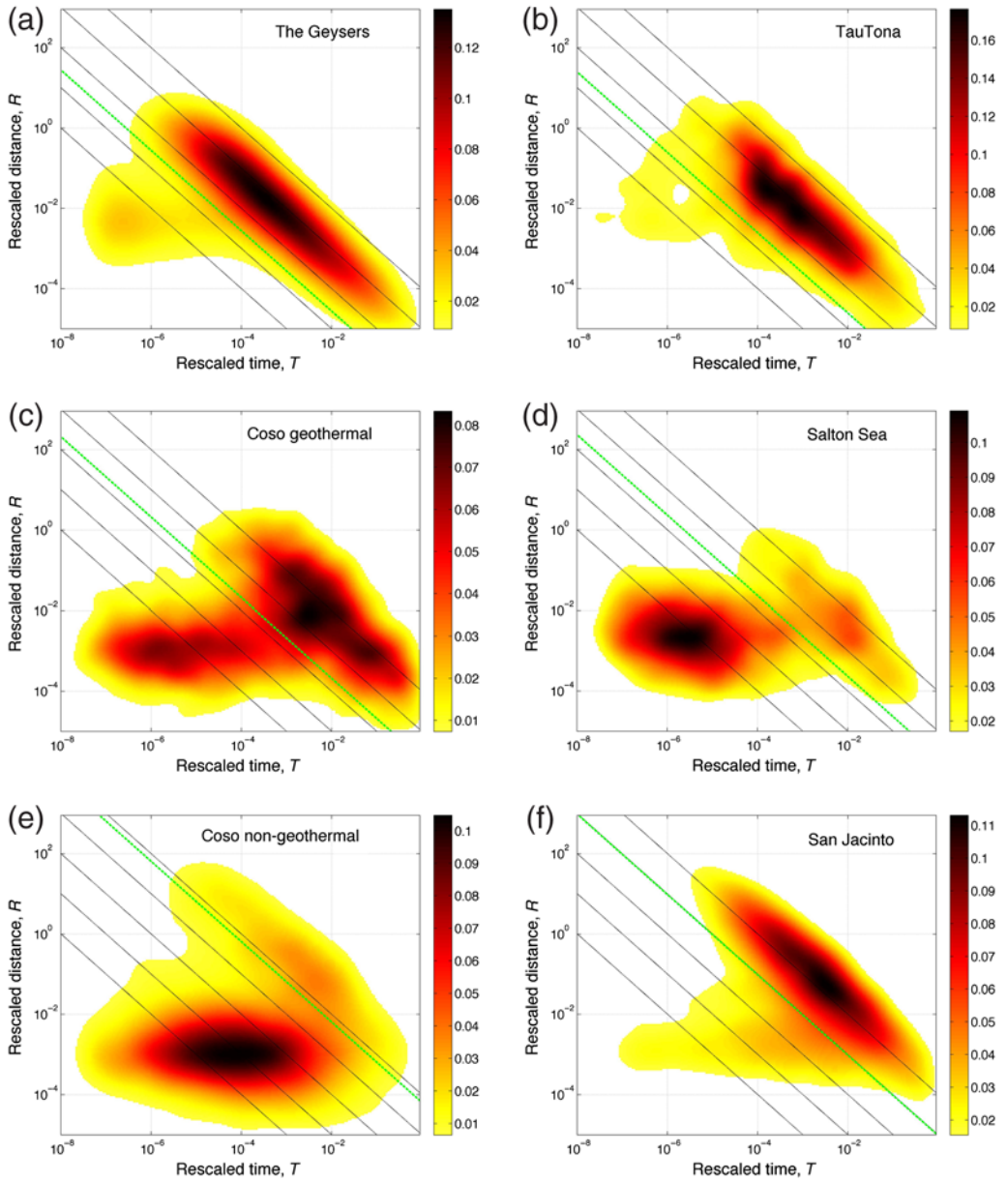

Figure 1. (a–f) Clustering style of seismicity in the six examined regions. Each panel shows the joint 2D distribution of the rescaled time T and distance R to the parent in a selected region. In TauTona, we only show events that happened between 00:00 and 13:00, when the mining activity is minimal. The solid diagonal lines are the same in all panels and correspond (from bottom to top) to $\eta = 10^{-8}$, 10^{-7}, 10^{-6}, 10^{-5}, and 10^{-4}. The dashed diagonal line depicts the mode separation threshold $\log_{10}\eta_0$ (also reported in Table 2). The sidebar indicates the density values. For visual convenience, we cut the lower 5% of each distribution (transparent background). The color version of this figure is available only in the electronic edition.

largely varying proportions of events attributed to each mode. The background mode in all panels is shaped as a diagonal ellipsoid along a line $\log_{10} T + \log_{10} R = \log_{10}\eta_B$. The rate of seismicity, dominated by the low-magnitude earthquakes, controls the proximity of the background mode to the origin (i.e., the value of the η_B) (Zaliapin *et al.*, 2008; Hicks, 2011). For instance, in The Geysers geothermal area (Fig. 1a), the background mode is located at $\log_{10}\eta_B \approx -5.2$, whereas in the San Jacinto region (Fig. 1f), the background mode is located further away from the origin at $\log_{10}\eta_B \approx -3.8$. This reflects a much higher seismicity rate in The Geysers compared with the San Jacinto region. The points between the origin and the background mode correspond to the clustered mode of seismicity. Table 2 summarizes information on the location and proportion of events for the cluster and background modes in the six examined regions. The background (clustered) events are defined here by the condition $\eta_{ij} > \eta_0 (\eta_{ij} \le \eta_0)$, with the threshold value η_0 estimated using a 1D Gaussian mixture model applied to the logarithmic nearest-neighbor distances $\log_{10}\eta_{ij}$ (Hicks, 2011). The characteristic location of the background mode is defined as $\log_{10}\eta_B = \text{Average}(\log_{10}\eta_{ij})$, with the average taken over all the background events. We

Table 2
Basic Characteristics of Background and Cluster Populations

Region	Mode Separation Threshold, $\log_{10}\eta_0$*	Background Proportion, P_B	Background Location, $\log_{10}\eta_B$	Cluster Proportion, $P_C = 1 - P_B$
The Geysers	−6.56	0.83	−5.20	0.17
TauTona†	−6.61	0.88	−5.11	0.12
Coso geothermal	−5.68	0.56	−4.21	0.44
Salton Sea	−5.63	0.31	−4.36	0.69
Coso nongeothermal	−4.19	0.18	−3.36	0.82
San Jacinto fault zone	−5.01	0.66	−3.79	0.34

*Estimated using the 1D Gaussian mixture model (Hicks, 2011).
†These estimations only use events between midnight and 1 p.m., when the blasting activity is minimal.

observe that the proportion of events in the background mode within the regions of induced seismicity (Fig. 1a,b) is higher than that in the other examined regions (c–f).

Taking a closer look at the background mode we notice that its extent along the line $\log_{10} T + \log_{10} R = \log_{10}\eta_B$ differs from region to region. In particular, in the areas of induced seismicity (The Geysers and TauTona), the background prominently extends into the lower-right corner of the (T, R) plane associated with large values of normalized interevent times T and small values of normalized interevent distances R. The areas of tectonic seismicity (Coso nongeothermal region and San Jacinto fault zone) have visible lack of events in this domain, whereas the areas of mixed seismicity (Coso geothermal and Salton Sea regions) are in between.

Different regions also have different extents of the background mode into the upper-left domain characterized by large R and small T values, although this difference is mainly controlled by the size of the geographic region and is less relevant to our discussion. In contrast, the observed differences in the large-T, small-R domain cannot be explained by differences in the space–time dimensions of a region. Indeed, most examined catalogs have comparable duration, except for TauTona, which has much shorter duration (see Table 1). However, TauTona is one of the regions that have a high concentration of events in the large-T, small-R domain; this indicates that the time interval of the examined catalog does not control this particular property of the background seismicity mode.

Next we observe that in areas of dominant induced seismicity (e.g., The Geysers), the clustered events are located at very short rescaled times ($T < 10^{-5}$) and relatively large rescaled distances ($R \approx 10^{-2}$) from the parents. On the other hand, in areas of dominant tectonic seismicity (e.g., San Jacinto), the clustered mode is concentrated at much longer rescaled times ($T \approx 10^{-4}$) and much shorter rescaled distances ($R \approx 10^{-3}$). The areas of mixed seismicity have intermediate position of the clustered mode. It is also seen that the separation of the background and clustered modes decreases from induced to mixed to tectonic regions. For instance, in The Geysers, the peak intensities of the clustered and background modes are separated by over an order of magnitude spacing in the (T, R) plane. However, in the San Jacinto area, the clustered mode is fused into the background mode without a clear separation.

To verify that these observations are not controlled by the overwhelming number of offspring of the few largest regional events, we repeated the analysis using only offspring with magnitudes within $\Delta = 1$ and $\Delta = 2$ units of the parent magnitude. Zaliapin and Ben-Zion (2013a) demonstrated that this approach (called Δ analysis) equalizes the number of offspring for events of different magnitudes in the 1981–2011 southern California catalog of Hauksson *et al.* (2012). The Δ analysis produces results very similar to those of Figure 1 and supports the observations described in this section. The results corresponding to $\Delta = 1$ are shown in Ⓔ Figure S3.

To verify the robustness of our observations on induced-clustering style, we performed additional analyses in the TauTona area. The TauTona catalog covers a geographic region that extends beyond the TauTona gold mine (see Ⓔ Fig. S2b), and hence includes events in close proximity as well as at a distance from the blasting. Furthermore, the main blasting activity in TauTona happens between 13:00 and 00:00, with prominent peak during 18:00–19:00, while blasting during the rest of the day is minimal (e.g., Boettcher *et al.*, 2015). This allows us to check the cluster style of TauTona induced seismicity in four types of space–time domains, characterized by mine proximity (within or outside) and blasting activity (active or minimal). In this article, we show results for time periods with minimal blasting activity and all spatial range. However, the cluster style remains very similar for the other examined subcatalogs (not shown). In particular, the increased distance-to-parent, faster temporal decay, and increased proportion of background events are observed in all examined subcatalogs.

Interpretation of Cluster Style

Our observations on the cluster style of the different examined regions may be explained conceptually in terms of the regional stress field. A typical tectonic region is expected to have an overall stress level that is relatively close to failure, corresponding roughly to the spatially varying strength threshold minus a fraction (e.g., 0.5) of a typical stress drop, superposed with a wide range of fluctuations produced by the long-term ongoing seismicity of different sizes (e.g., Ben-Zion *et al.*, 2003; Bailey and Ben-Zion, 2009). Accordingly,

the static and dynamic stress redistribution caused by an earthquake easily triggers offspring events in the immediate vicinity of the parent (where the offspring rate prominently peaks) as well as further away in space and time with declining rate. Furthermore, postseismic dynamic processes, aided by the highly inhomogeneous stress field, lead to continuing triggering of offspring events near the parents for a long time.

In contrast, an area with dominant induced seismicity is primarily disturbed by local fluid injection and/or extraction or by blasting activities, so it is likely to have fluctuating and close-to-failure stress only locally rather than over a large scale as in tectonic regions, with stress heterogeneities covering a narrower range than in tectonic regions. Accordingly, larger distances are required statistically to encounter places with near-threshold initial stress for earthquake-related stress redistribution to be efficient in generating offspring events. Also, the triggering activity decays relatively fast in time because of the absence of many locations with near-threshold stress that can produce events in response to postseismic processes.

Our interpretation of cluster style suggests a shorter duration and more diffuse cluster activity in induced earthquakes, which is well supported by the cluster results in The Geysers and TauTona areas (see Fig. 1, Table 2, and Ⓔ Fig. S3). The same interpretation also implies that the background-to-cluster proportions in induced regions are higher than in areas of natural seismicity. However, this claim cannot be tested rigorously by the current analysis of spatially distinct regions, where the background-to-cluster proportions are affected by a multitude of other conditions besides the principal seismic driver. We will confirm this claim below in the Temporal Change of Cluster Style in Coso and Salton Sea Geothermal Fields section by analyzing the temporal evolution of clustering in the two regions with mixed seismicity.

The extended portion of the background domain characterized by low-R and large-T values corresponds to events that happen within the rupture area of some previous earthquakes at times much exceeding typical duration of an aftershock series. Such events can generally be labeled as repeaters. Although repeaters are abundant on the creeping section of the San Andreas fault (Nadeau and McEvilly, 1997; Rubin and Gillard, 2000) and other relatively smooth faults with a mixture of brittle and creeping patches (Ben-Zion and Sammis, 2003; McGuire, 2008), they are less common on most tectonic faults. This is evident, for example, for the San Jacinto and nongeothermal Coso regions, in the results of Figure 1 and Ⓔ Figure S3. On the other hand, repeaters are favored in induced seismicity, because in such areas imposed loadings such as fluid injections/withdrawal and blast activities occur repeatedly at the same locations (Fig. 1a,b). Interestingly, the results of Figure 1 and Ⓔ Figure S3 also suggest that typical cluster activity in areas of induced seismicity happens at larger distances from the parent than repeater activity. In the examined areas of tectonic seismicity, the lower limits of the spatial separation between parents and offspring are (almost) the same for clustered events and repeaters.

Quantification of Cluster Style

Here, we propose a quantitative approach that emphasizes the differences in the cluster styles of seismicity in the examined induced and tectonic areas. A useful statistic that combines several of the cluster style properties described above is the relative location of the clustered mode with respect to the background mode. This can be measured by the relative quantile approach that focuses exclusively on the relative positions of the different modes rather than on their absolute (T, R) coordinates. Recall that an empirical distribution function $F(x)$ for a sample $\{x_1, \ldots, x_n\}$ is defined as

$$F(x) = \frac{\#\{i : x_i \le x\}}{n}, \qquad -\infty < x < \infty. \tag{6}$$

Here $\#\{A\}$ denotes the number of elements in set A. Let F_T and F_R be the empirical distribution functions of the rescaled time T and distance R to the parent, respectively, computed for the background events. The relative quantiles for an event with rescaled time T_i and distance R_i to the parent are defined as $Q_T = F_T(T_i)$ and $Q_R = F_R(R_i)$.

Figure 2 shows the joint distribution of the defined relative quantiles (Q_T, Q_R) computed for all the clustered events and the respective marginal distribution of Q_R (as an inset). Areas with induced seismicity (Fig. 2a,b) are characterized by high concentration of Q_T in the vicinity of zero, which reflects the fact that the duration of a typical cluster is much shorter than parent–offspring interevent times in the background mode. Induced seismicity areas also exhibit relatively high values of Q_R, with median within the interval 0.3–0.4 (see insets), which reflects the fact that the spatial separation of parents and offspring in clusters is comparable with that of background events. This also signifies the existence of repeaters—events whose distance to parent is much smaller than a typical distance to parent in a cluster. In contrast, the areas with natural tectonic seismicity (Fig. 2e,f) show a substantial spread of the Q_T values (much longer offspring duration) and high concentration of Q_R near the origin (spatial separation of parents and offspring in clusters is much smaller than background events). The cluster style in areas of mixed seismicity (Fig. 2c,d) is in between the clear-cut styles in induced and tectonic areas. The relative quantile approach corroborates the initial observations of Figure 1, while making the differences between cluster styles of different environments more visible.

Figure 3 emphasizes the differences between cluster styles of induced and tectonic activity by showing the distribution of the rescaled time T to parent for events that occurred within one parent rupture length from the parent. We estimate the rupture length of a magnitude m event using the formula for crack-like events with circular areas (Ben-Zion, 2008):

$$L_m = 0.0152 \times 10^{0.42m}. \tag{7}$$

This approximation works well for events with $m < 5.5$ and somewhat underestimates the rupture lengths of larger events

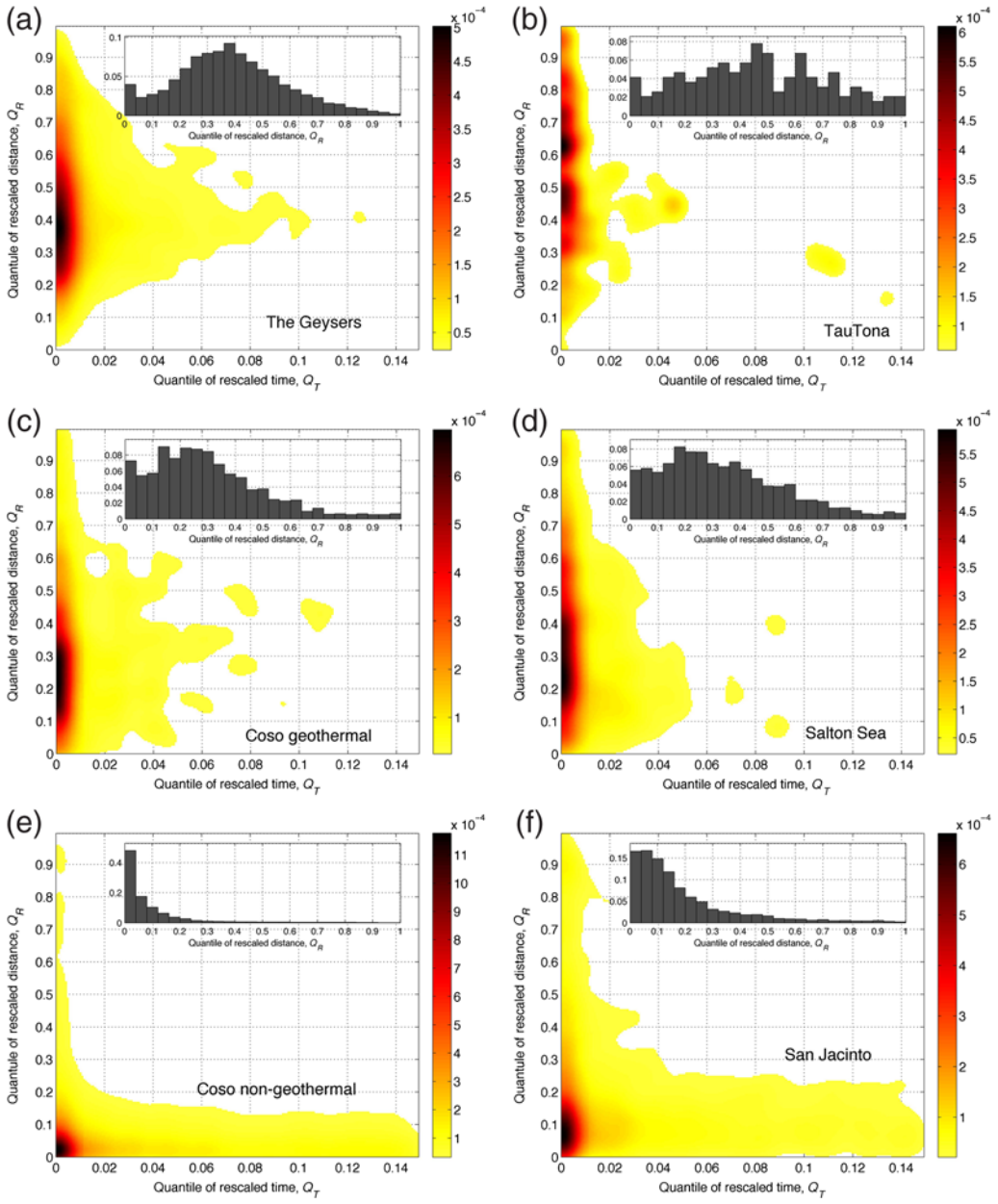

Figure 2. (a–f) Cluster style of seismicity in the six examined regions via the relative quantile approach. Each panel shows the joint distribution of the relative quantiles (Q_T, Q_R) in a selected region. The insets show the marginal distribution of Q_R. For visual convenience, we cut the lower 20% of each distribution. The color version of this figure is available only in the electronic edition.

(compare with fig. 6 of Ben-Zion, 2008). In the areas of induced seismicity (Fig. 3a,b), as well as in the areas of mixed seismicity (Fig. 3c,d), there is a strongly bimodal distribution of the rescaled times to parent. The left mode (shorter values of T) corresponds to earthquake clusters and is well separated from the right mode (larger values of T) that corresponds to background events (repeaters). The existence and good separation of the two modes indicates that a typical cluster occupies an exclusive spatiotemporal domain around the parent and has a little overlap with background seismicity. In contrast, the distribution of T in tectonic regions (Fig. 3e,f) is unimodal. This occurs because the peak of offspring activity happens later in time after the parent and the offspring activity decays rather slowly, allowing the tail of a typical cluster to merge with the background seismicity.

The temporal decay of the offspring in the six examined regions is compared in Figure 4; the figure shows the estimated density of close offspring (those with $\eta_{ij} < \eta_0$) as a function of time after the parent. This analysis supports the observations made in Figures 1–3: the offspring in areas of induced seismicity tend to decay much faster than in tectonic areas; the temporal decay of the offspring intensity $\Lambda(t)$ in all examined regions is closely approximated by a power law $\Lambda(t) \propto t^{-h}$; and the power exponent changes from $h \approx 2$ in induced areas to $h \approx 1.5$ in the mixed regions and to $h \approx 1$ in tectonic regions.

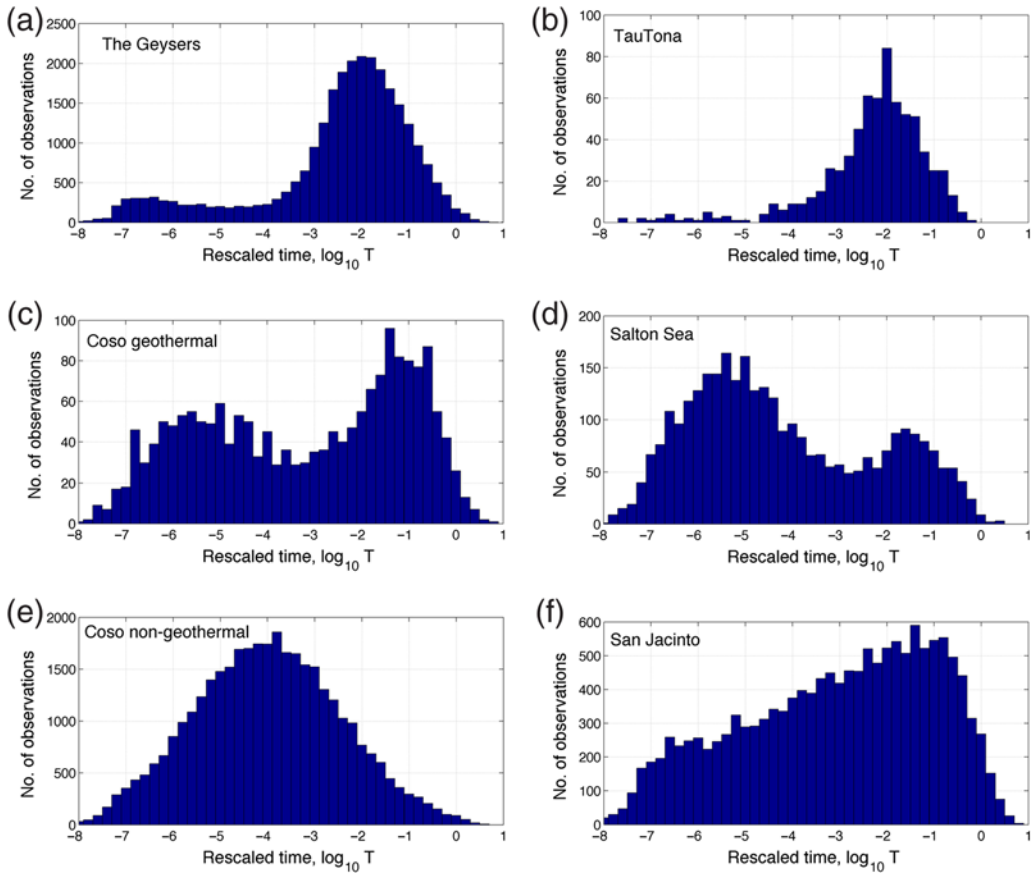

Figure 3. Distribution of rescaled time for the offspring within one parent rupture length from the parent. Notice (a–d) bimodal distribution of the rescaled times in induced and mixed regions versus (e,f) unimodal distribution in tectonic regions. The color version of this figure is available only in the electronic edition.

Temporal Change of Cluster Style in Coso and Salton Sea Geothermal Fields

The differences in cluster styles reported above may characterize particular instances of tectonic versus induced seismicity associated with the chosen regions. However, these results alone cannot be used to claim that the differences are caused by the different types of seismic drivers. Instead, they might be due to different physical environments, differences in earthquake reporting, and other details specific to the example regions. For instance, several aspects of seismic clustering in southern California were shown to be tightly related to the effective viscosity of the crust and to change on scales of tens of kilometers (Zaliapin and Ben-Zion, 2013b). In addition, inferred clustering properties are affected by various catalog uncertainties that can lead to spurious fluctuations of parent–offspring distances and other artifacts (Zaliapin and Ben-Zion, 2015). Therefore, the observed differences between tectonic and induced areas discussed so far may be attributed to significantly different levels of heat flow, different earthquake location quality, etc. To rule out these possibilities, we analyze temporal changes in two regions, the Coso and Salton Sea geothermal fields, where the start of significant geothermal production happened within the span of available high-quality catalogs. The physical properties and catalog compilation factors in each region remained similar, allowing a focus on changes associated with the principal seismic driver.

It is well known that the seismicity in both the Coso and Salton Sea geothermal fields experienced a noticeable change after the beginning of geothermal production in these areas in 1987 and 1988, respectively (e.g., Brodsky and Lajoie, 2013). The change in cluster production and seismic intensity is illustrated in Figure 5, which shows a 1D spatial coordinate of events as a function of time. In both regions, seismicity transitions from a sequence of rare, highly clustered, and well-separated sequences to numerous individual events and small clusters that occur in the vicinity of the geothermal production well heads.

Figure 6 presents the joint distribution of the rescaled time and distance to parent (Fig. 6a,b) and its relative quantile version (Fig. 6c,d) before (Fig. 6a,c) and after (Fig. 6b,d) the launch of geothermal production in the Coso geothermal field. The results show a substantial shift in the distribution of the distance-to-parent in both absolute (R) and relative (Q_R) expressions, associated with the onset of geothermal activity. In addition, the figure clearly demonstrates the convenience of the relative location approach: the change of the background

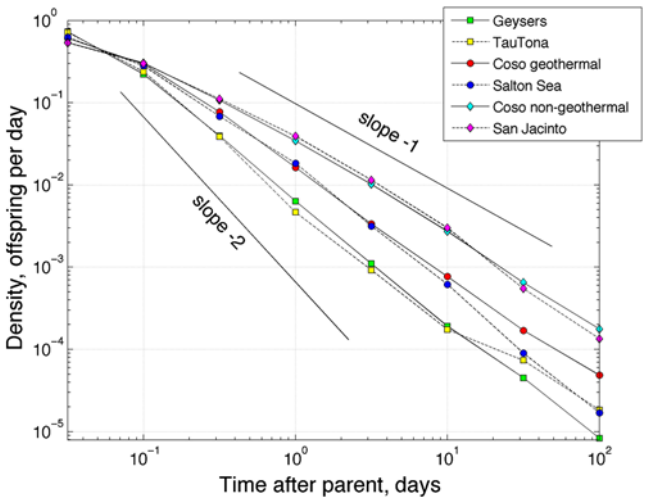

Figure 4. Temporal decay of the offspring intensity. Normalized intensity (average number of offspring per parent per day, scaled to integrate to unity) as a function of time t after the parent. Analysis uses all close offspring ($\eta < \eta_0$). The color version of this figure is available only in the electronic edition.

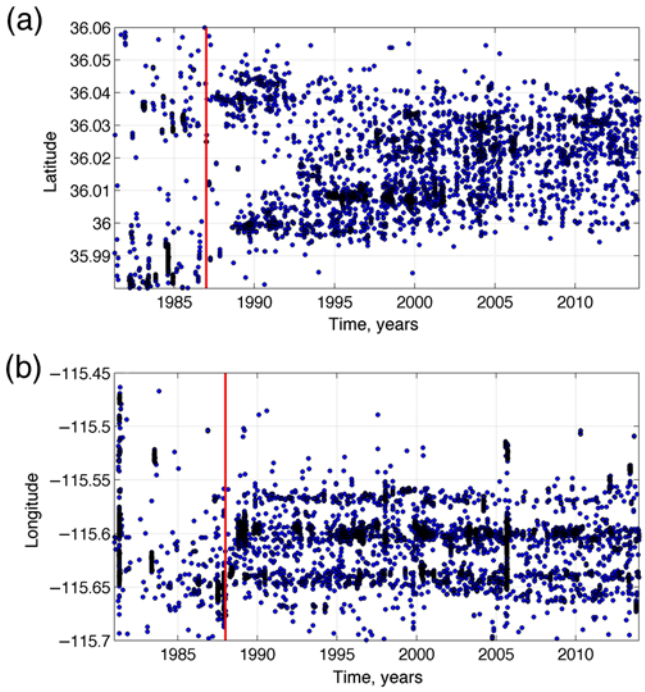

Figure 5. Transition from tectonic to induced seismicity in (a) Coso and (b) Salton Sea geothermal fields. The figure shows a 1D coordinate of the earthquakes as a function of time. The vertical lines mark the onset of active geothermal production. The color version of this figure is available only in the electronic edition.

distribution, shifted toward longer times and shorter distances after 1987 (compare with Fig. 6a and 6b), makes the differences between Figure 6c and 6d more eye-catching than those between Figure 6a and 6b, although both sets of panels refer to the same data set. The results of the same analysis for the Salton Sea geothermal field (Fig. 7) also document a notable change of the clustering style of seismicity after the geothermal production expansion of 1988–1992.

Figures 6 and 7 show that transition from tectonic to human-induced earthquakes in the Coso and Salton Sea geothermal fields leads to an increase in both the proportion of the background events and the absolute intensity of the background events, as well as to more rapid temporal offspring decay. These observations are further confirmed by an analysis (Fig. 8) that compares the distribution of the rescaled time T to parent in the Coso and Salton Sea geothermal fields prior to and after the expansion of the geothermal production. Both regions exhibit a clear transition from a unimodal distribution of T with slow temporal decay in clusters and undeveloped background mode to a bimodal distribution with a clear separation between clustered and background (having many repeaters) modes and a fast temporal offspring decay in clusters. Recall that the same transition was reported in Figure 3 for tectonic versus induced regions.

Figure 9 illustrates differences in the dynamics of the background population in the Coso geothermal and nongeothermal areas during 1981–2014. The analysis is done in a moving window of five years, and the results are shown for the interval (1986–2014); the first point corresponds to the first full window of five years. This analysis reflects the changes associated with transition from tectonic-dominated to induced-dominated seismicity in the Coso geothermal field. In this region, the background proportion jumps from $P_B \approx 0.25$ to $P_B \approx 0.6$ in 1989 and stays at this high level thereafter. The transition point corresponds to the time interval (1984–1989), which covers the onset of geothermal production. Notably, the background proportion remains relatively constant (with some minor fluctuations) in the nongeothermal Coso area. Assuming that the physical regional properties and catalog reporting are comparable for these two geographically close areas, the result of Figure 9 further supports our claim that the changes reported for the Coso geothermal field are due to the changing type of seismic drivers from tectonic to human induced.

We note that large earthquake clusters virtually disappear in both the Coso and Salton Sea geothermal regions after the beginning of geothermal production (Fig. 5) and are replaced with numerous smaller clusters. Figure 10 shows the distribution of cluster sizes in both areas before and during geothermal production (Fig. 10a,b). The cluster is defined as a union of events connected by short ($\eta_{ij} \le \eta_0$) links to parent. Specifically, a cluster always starts with a background event and consists of close offspring of this event, close offspring of these offspring, etc. (see Zaliapin and Ben-Zion, 2013a, for further detail of this definition). The distribution of cluster size N in all examined cases has a roughly power-law tail,

$$\Pr[N > x] \propto x^{-s}, \tag{8}$$

with exponent s that is significantly smaller during the tectonic period ($s \approx 1$) than during the induced seismicity period ($s \approx 2$). The same general tendency (i.e., decrease of power

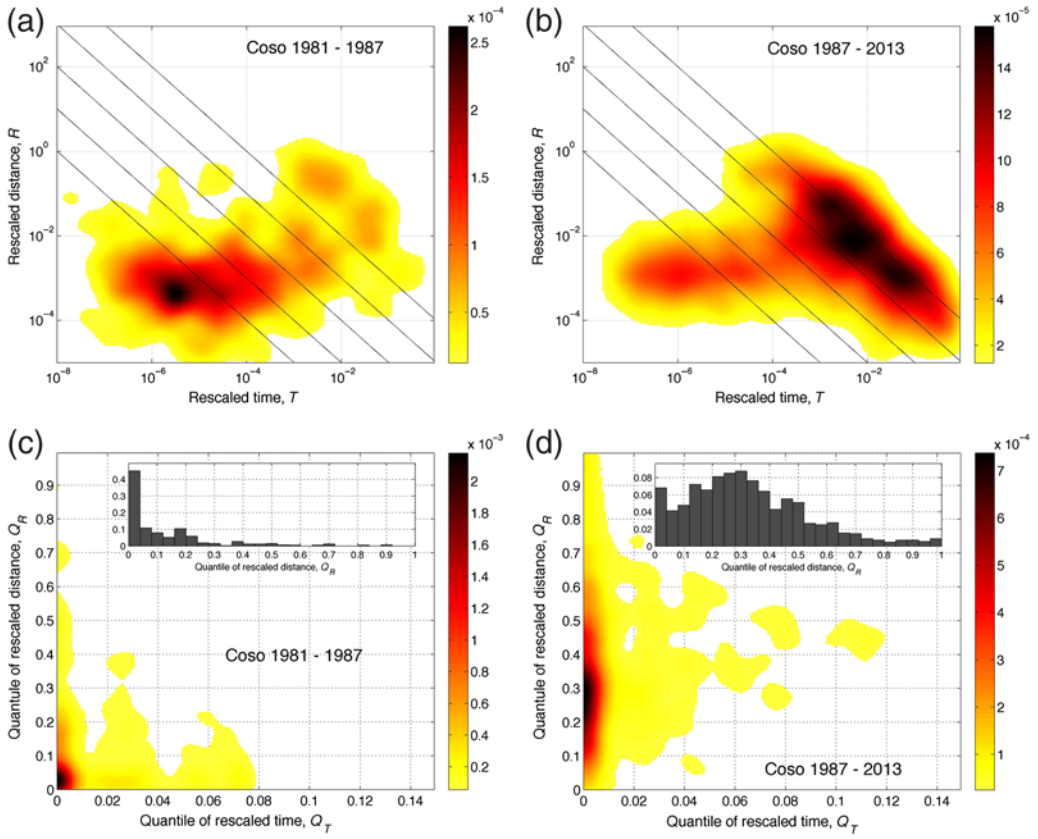

Figure 6. Clustering style in Coso geothermal area (a,c) before and (b,d) after the expansion of the geothermal production in 1987. (a,b) Joint distribution of the rescaled components (T, R) of the nearest-neighbor distance η; for visual convenience, we cut the lower 5% of each distribution. (c,d) Joint distribution of the relative quantiles (Q_T, Q_R). The insets show the histogram of Q_R; for visual convenience, we cut the lower 20% of each distribution. The color version of this figure is available only in the electronic edition.

law exponent for induced seismicity) is seen for the four clear-cut regions (Fig. 10c): The Geysers ($s \approx 3$), TauTona ($s \approx 3$), Coso nongeothermal ($s \approx 1$), and San Jacinto ($s \approx 1.5$). A closer and more formal examination of the cluster size distribution in tectonic and induced seismicity will be done in a follow up work.

Discussion

We attempt to distinguish between seismicity produced by tectonic loads and seismicity caused by human activities such as geothermal production and blasting, based on statistical characterization of clusters and background events. The separation between these two modes of events is done with analysis of nearest-neighbor distances in combined space–time–magnitude coordinates (equations 1 and 5). We focus on a small number of selected regions with clear-cut and well-documented types of tectonic versus induced seismic drivers. Two of the regions have a change within the analyzed time interval from tectonic-dominated to induced-dominated seismicity.

The results (Figs. 1–3) suggest that induced seismicity has (1) higher background intensity (expressed in both the proportion of background events and intensity of background events); (2) faster temporal decay of offspring, which might be expressed either via a higher exponent h of power-law offspring intensity decay $\Lambda(t) \propto t^{-h}$ (Fig. 4) or via the existence of a bimodal distribution of rescaled time to parent in the vicinity of the parent (Fig. 3); (3) higher rate of repeaters, that is, earthquakes that occur in a close vicinity of a previous event and at times much larger than those of aftershock series (Fig. 1); (4) larger proportion of small clusters (Fig. 10); and (5) statistically larger distance between parent and offspring (Fig. 1). A physical interpretation of these findings is suggested in the Interpretation of Cluster Style section, based on the expected large-scale level and range of heterogeneities of the stress field. The findings are further supported by analysis of temporal changes of the style of seismicity in two regions that experienced development of geothermal production within the time covered by the high-quality catalogs, the Coso and Salton Sea geothermal fields (Figs. 6–9). This later analysis provides a natural control for various regional and catalog reporting properties, which cannot be achieved in the analysis of distinct regions. The results provide a stronger confidence that the reported changes are due to different seismic drivers.

The observations presented in this study are neither intended nor able to fully characterize areas of induced seismicity. It is possible that there are tectonic regions with

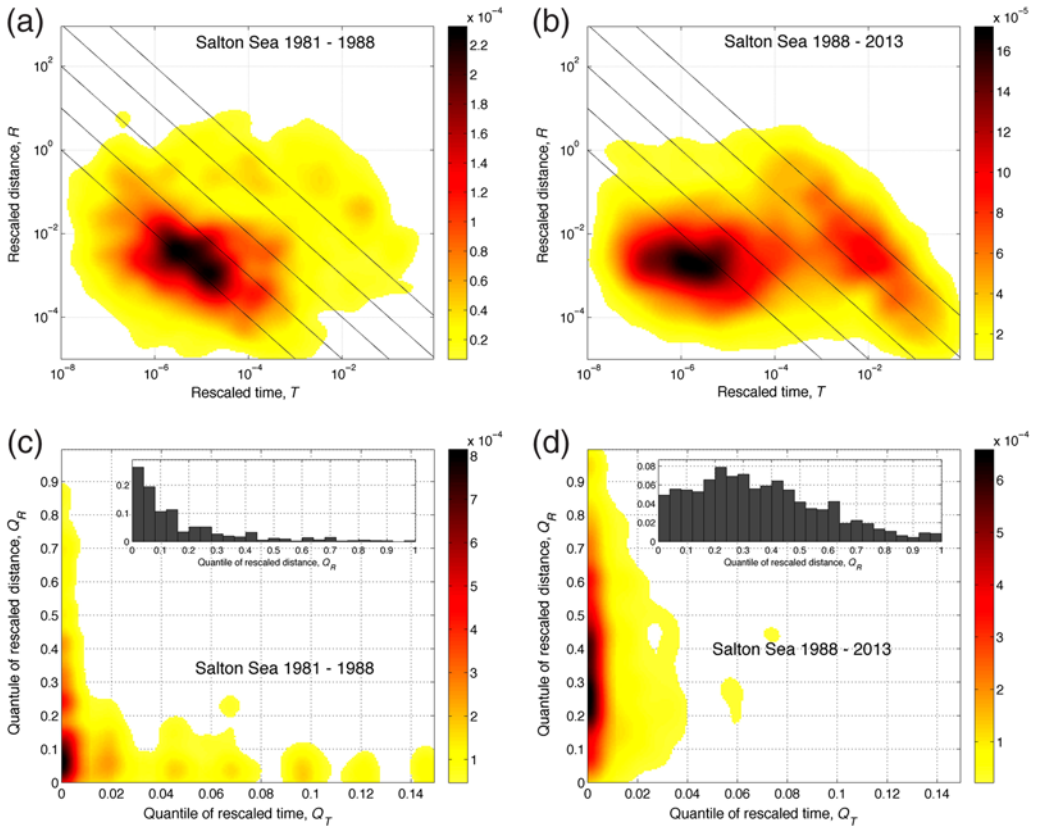

Figure 7. Clustering style in the Salton Sea geothermal area (a,c) before and (b,d) after the expansion of geothermal production during 1988–1992. (a,b) Joint distribution of the rescaled components (T, R) of the nearest-neighbor distance η; for visual convenience, we cut the lower 2% of each distribution. (c,d) Joint distribution of the relative quantiles (Q_T, Q_R). The insets show the histogram of Q_R; for visual convenience, we cut the lower 20% of each distribution. The color version of this figure is available only in the electronic edition.

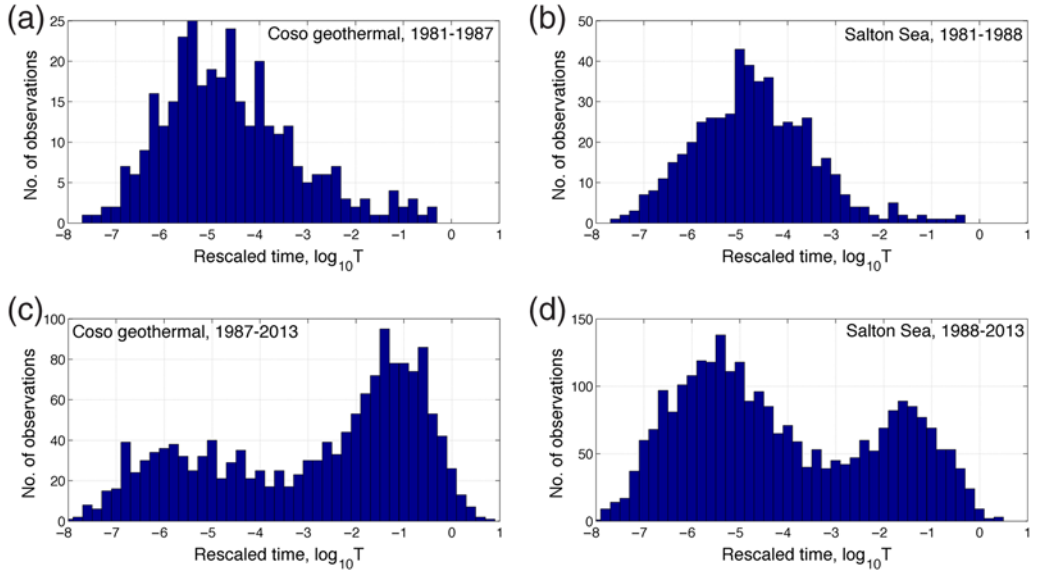

Figure 8. Change of clustering style in Coso and Salton Sea geothermal fields after the beginning of active geothermal production. The figure shows the distribution of the rescaled time to parent T for the offspring within one parent rupture length from the parent. (a,c) Coso geothermal field; production began in 1987. (b,d) Salton Sea geothermal field; production began during 1988–1992. (a,b) Offspring before geothermal production. (c,d) Offspring during geothermal production. The color version of this figure is available only in the electronic edition.

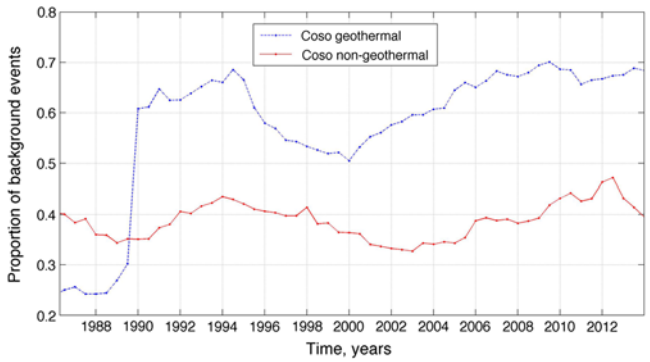

Figure 9. Proportion of background events as a function of time in Coso geothermal (dashed) and Coso nongeothermal (solid) areas. The proportion is estimated in a five-year moving window. The results are shown at the end of the window; hence the point at 1990 corresponds to the interval (1985–1990), etc. Notice the abrupt increase of background events in the Coso geothermal area in 1989 that corresponds to the interval (1984–1989) and is associated with the onset of geothermal production. The color version of this figure is available only in the electronic edition.

particular combinations of physical characteristics, loadings, and catalog uncertainties that can produce cluster style similar to that of the induced seismicity regions analyzed here. For example, Ⓔ Figure S4 shows the cluster style of seismicity in the Parkfield area based on the relocated catalog of Waldhauser and Schaff (2008). The earthquakes in that region are tectonically driven, but, in agreement with previous studies (e.g., Nadeau and McEvilly, 1997), we observe (Fig. S4a) that the Parkfield seismicity features unusually high intensity of repeaters. This produces (Fig. S4b) a cluster style similar to that observed in the areas of mixed seismicity (the Coso and Salton Sea geothermal areas). However, the rescaled times to parent (Fig. S4c) show a unimodal distribution caused by a slow temporal offspring decay rate that leads to blending of the cluster and background (repeater) modes. This is indeed one of the features attributed to tectonic seismicity in our analysis above. This example emphasizes that distinguishing between natural and induced seismicity requires multiple signals (e.g., high proportion of repeaters and fast temporal decay of offspring events).

It is also important to emphasize that various catalog uncertainties create notable pitfalls in estimating earthquake cluster properties, which also might affect the discrimination studies. In particular, increased earthquake location errors lead to artificially increased background rates and increased spatial separation between parent and offspring (Zaliapin and Ben-Zion, 2015). This implies that low-quality catalogs may create artificial cluster patterns reminiscent of those observed in induced seismicity areas.

The catalogs examined in this study are also subject to varying location quality (e.g., Zaliapin and Ben-Zion, 2015). In particular, it is known that the TauTona catalog quality rapidly decays away from the mine (M. Boettcher, personal comm., 2015). To ensure that our results are not affected by the space-dependent catalog properties, we repeated the analyses for different selections of subcatalogs in every examined region. These results (not shown) are very similar to the main findings documented and illustrated in this study, supporting our main conclusions.

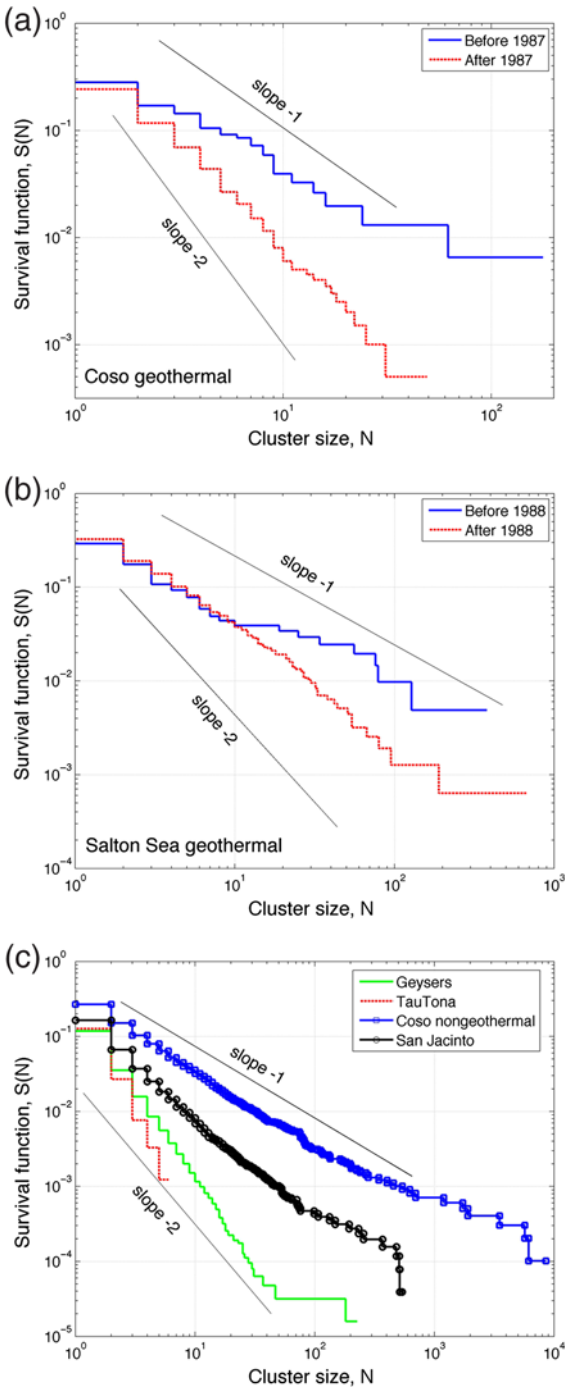

Figure 10. Distribution of cluster size. (a) Coso geothermal region before (solid) and after (dashed) expansion of geothermal production in 1987. (b) Salton Sea geothermal region before (solid) and after (dashed) expansion of geothermal production in 1988. (c) Other examined regions (from top to bottom): Coso nongeothermal, San Jacinto, The Geysers, and TauTona. Lines with slopes −1 and −2 are shown in each panel for visual convenience. The color version of this figure is available only in the electronic edition.

Summing up, a thorough regional analysis that incorporates catalog uncertainties is strongly advised in efforts to determine the genuine cluster style of a region before using the results of this study (or similar ones) to distinguish between tectonic and induced seismicity. Also, it is advisable to use a collection of complementary properties rather than to focus on any single one, even if the latter shows a good discrimination power in a particular region. Despite these cautionary remarks, we believe that the main qualitative findings of this study are useful for classifying and distinguishing seismicity in natural and induced regions. Developing additional discriminating signals (work in progress) will increase the robustness of characterizing the styles of seismicity in different regions.

Data and Resources

The waveform relocated earthquake catalog for southern California during 1981–2013 by E. Hauksson, W. Yang, and P. M. Shearer is available from http://www.data.scec.org/research-tools/downloads.html (last accessed November 2014). The TauTona catalog was provided to us by Margaret Boettcher. The other data used in this article came from published sources listed in the references. Some plots were made using Generic Mapping Tools v.4.5.8 (www.soest.hawaii.edu/gmt, last accessed July 2015; Wessel and Smith, 1991).

Acknowledgments

We thank Margaret Boettcher for providing us the TauTona catalog. The manuscript benefitted from useful comments by Margaret Boettcher, an anonymous reviewer, and Associate Editor Ivan Wong. The study was supported by the Southern California Earthquake Center (SCEC, based on National Science Foundation Cooperative Agreement EAR-1033462 and U.S. Geological Survey Cooperative Agreement G12AC20038). The SCEC Contribution Number for this article is 6183.

References

Baiesi, M., and M. Paczuski (2004). Scale-free networks of earthquakes and aftershocks, *Phys. Rev. E* **69,** 066106, doi: 10.1103/PhysRevE.69.066106.

Bailey, I. W., and Y. Ben-Zion (2009). Statistics of earthquake stress drops on a heterogeneous fault in an elastic half-space, *Bull. Seismol. Soc. Am.* **99,** 1786–1800, doi: 10.1785/0120080254.

Ben-Zion, Y. (2008). Collective behavior of earthquakes and faults: Continuum-discrete transitions, evolutionary changes and corresponding dynamic regimes, *Rev. Geophys.* **46,** RG4006, doi: 10.1029/2008RG000260.

Ben-Zion, Y., and C. G. Sammis (2003). Characterization of fault zones, *Pure Appl. Geophys.* **160,** 677–715.

Ben-Zion, Y., M. Eneva, and Y. Liu (2003). Large earthquake cycles and intermittent criticality on heterogeneous faults due to evolving stress and seismicity, *J. Geophys. Res.* **108,** no. B6, 2307, doi: 10.1029/2002JB002121.

Boettcher, M. S., D. L. Kane, A. McGarr, M. J. Johnston, and Z. E. Reches (2015). Moment tensors and other source parameters of mining-induced earthquakes in TauTona Mine, South Africa, *Bull. Seismol. Soc. Am.* **105,** 1576–1593, doi: 10.1785/0120140300.

Boettcher, M. S., A. McGarr, and M. Johnston (2009). Extension of Gutenberg–Richter distribution to M_w 1.3, no lower limit in sight, *Geophys. Res. Lett.* **36,** L10307, doi: 10.1029/2009GL038080.

Brodsky, E. E., and L. J. Lajoie (2013). Anthropogenic seismicity rates and operational parameters at the Salton Sea geothermal field, *Science* **341,** no. 6145, 543–546.

Chen, X., P. M. Shearer, and R. E. Abercrombie (2012). Spatial migration of earthquakes within seismic clusters in southern California: Evidence for fluid diffusion, *J. Geophys. Res.* **117,** no. B04301, doi: 10.1029/2011JB008973.

Daley, D. J., and D. Vere-Jones (2007). *An Introduction to the Theory of Point Processes: Volume II: General Theory and Structure*, Vol. 2, Springer Science and Business Media, New York.

Eberhart-Phillips, D., and D. H. Oppenheimer (1984). Induced seismicity in The Geysers geothermal area, California, *J. Geophys. Res.* **89,** no. B2, 1191–1207.

Ellsworth, W. L. (2013). Injection-induced earthquakes, *Science* **341,** doi: 10.1126/science.1225942.

Gu, C., A. Y. Schumann, M. Baiesi, and J. Davidsen (2013). Triggering cascades and statistical properties of aftershocks, *J. Geophys. Res.* **118,** 4278.

Hauksson, E., and J. Unruh (2007). Regional tectonics of the Coso geothermal area along the intracontinental plate boundary in central eastern California: Three-dimensional V_P and V_P/V_S models, spatial-temporal seismicity patterns, and seismogenic deformation, *J. Geophys. Res.* **112,** no. B06309, doi: 10.1029/2006JB004721.

Hauksson, E., T. Goebel, J.-P. Ampuero, and E. Cohran (2015). A century of oilfield operations and earthquakes in the greater Los Angeles basin, southern California, *TLE* **34,** no. 6, 650–656.

Hauksson, E., W. Yang, and P. M. Shearer (2012). Waveform relocated earthquake catalog for southern California (1981 to June 2011), *Bull. Seismol. Soc. Am.* **102,** no. 5, 2239–2244, doi: 10.1785/0120120010.

Hicks, A. (2011). Clustering in multidimensional spaces with applications to statistical analysis of earthquake clustering, *M.Sc. Thesis*, Department of Mathematics and Statistics, University of Nevada, Reno (August 2011).

Horton, S. (2012). Disposal of hydrofracking waste fluid by injection into subsurface aquifers triggers earthquake swarm in central Arkansas with potential for damaging earthquake, *Seismol. Res. Lett.* **83,** no. 2, 250–260.

Keranen, K. M., H. M. Savage, G. A. Abers, and E. S. Cochran (2013). Potentially induced earthquakes in Oklahoma, USA: Links between wastewater injection and the 2011 M_w 5.7 earthquake sequence, *Geology* **41,** no. 6, 699–702.

Lippmann-Pipke, J., J. Erzinger, M. Zimmer, C. Kujawa, M. Boettcher, E. Van Heerden, A. Bester, H. Moller, N. A. Stroncik, and Z. Reches (2011). Geogas transport in fractured hard rock–Correlations with mining seismicity at 3.54 km depth, TauTona gold mine, South Africa, *Appl. Geochem.* **26,** no. 12, 2134–2146.

Majer, E. L., and J. E. Peterson (2007). The impact of injection on seismicity at The Geysers, California geothermal field, *Int. J. Rock Mech. and Mining Sci.* **44,** no. 8, 1079–1090.

Marks, S. M., R. S. Ludwin, K. B. Louie, and C. G. Bufe (1978). Seismic monitoring at The Geysers geothermal field, California, *U.S. Geol. Surv. Open File Rept. 78-798*, 26 pp.

McGarr, A. (1991). On a possible connection between three major earthquakes in California and oil production, *Bull. Seismol. Soc. Am.* **81,** 948–970.

McGarr, A., D. Simpson, and L. Seeber (2002). Case histories of induced and triggered seismicity, in *International Handbook of Earthquake and Engineering Seismology*, W. H. Lee, P. Jennings, C. Kisslinger, and H. Kanamori (Editors), Vol. 81A, Academic Press, London, United Kingdom, 647–661.

McGuire, J. J. (2008). Seismic cycles and earthquake predictability on East Pacific Rise transform faults, *Bull. Seismol. Soc. Am.* **98,** no. 3, 1067–1084.

Nadeau, R. M., and T. V. McEvilly (1997). Seismological studies at Parkfield V: Characteristic microearthquake sequences as fault-zone drilling targets, *Bull. Seismol. Soc. Am.* **87,** 1463–1472.

Oppenheimer, D. H. (1986). Extensional tectonics at The Geysers geothermal area, California, *J. Geophys. Res.* **91,** no. B11, 11,463–11,476.

Rubin, A. M., and D. Gillard (2000). Aftershock asymmetry/rupture directivity among central San Andreas fault microearthquakes, *J. Geophys. Res.* **105,** 19,095–19,109.

Suckale, J. (2010). Moderate to large seismicity induced by hydrocarbon production, *TLE* **29,** no. 3, 310–319, doi: 10.1190/1.3353728.

Vidale, J. E., and P. M. Shearer (2006). A survey of 71 earthquake bursts across southern California: Exploring the role of pore fluid pressure fluctuations and aseismic slip as drivers, *J. Geophys. Res.* **111,** no. B5, B05312, doi: 10.1029/2005JB004034.

Waldhauser, F., and D. P. Schaff (2008). Large-scale relocation of two decades of northern California seismicity using cross-correlation and double-difference methods. *J. Geophys. Res.* **113,** no. B08311, doi: 10.1029/2007JB005479.

Wessel, P., and W. H. Smith (1991). Free software helps map and display data, *Eos Trans. AGU* **72,** no. 441, 445–446.

Zaliapin, I., and Y. Ben-Zion (2011). Asymmetric distribution of aftershocks on large faults in California, *Geophys. J. Int.* **185,** no. 3, 1288–1304.

Zaliapin, I., and Y. Ben-Zion (2013a). Earthquake clusters in southern California I: Identification and stability, *J. Geophys. Res.* **118,** no. 6, 2847–2864.

Zaliapin, I., and Y. Ben-Zion (2013b). Earthquake clusters in southern California II: Classification and relation to physical properties of the crust, *J. Geophys. Res.* **118,** no. 6, 2865–2877.

Zaliapin, I., and Y. Ben-Zion (2015). Artefacts of earthquake location errors and short-term incompleteness on seismicity clusters in southern California, *Geophys. J. Int.* **202,** 1949–1968, doi: 10.1093/gji/ggv259.

Zaliapin, I., A. Gabrielov, V. Keilis-Borok, and H. Wong (2008). Clustering analysis of seismicity and aftershock identification, *Phys. Rev. Lett.* **101,** 018501, doi: 10.1103/PhysRevLett.101.018501.

Department of Mathematics and Statistics
University of Nevada
Reno, Nevada 89557
zal@unr.edu
(I.Z.)

Department of Earth Sciences
University of Southern California
Los Angeles, California 90089
benzion@usc.edu
(Y.B.-Z.)

Manuscript received 18 February 2016;
Published Online 12 April 2016